NANO LETTERS

pubs.acs.org/NanoLett

Letter

Chemomechanically Stable Ultrahigh-Ni Single-Crystalline Cathodes with Improved Oxygen Retention and Delayed Phase Degradations

Chunyang Wang, Rui Zhang, Carrie Siu, Mingyuan Ge, Kim Kisslinger, Youngho Shin,*
and Huolin L. Xin*

Cite This: https://doi.org/10.1021/acs.nanolett.1c03852

Read Online

ACCESS | Metrics & More | Article Recommendations | Supporting Information

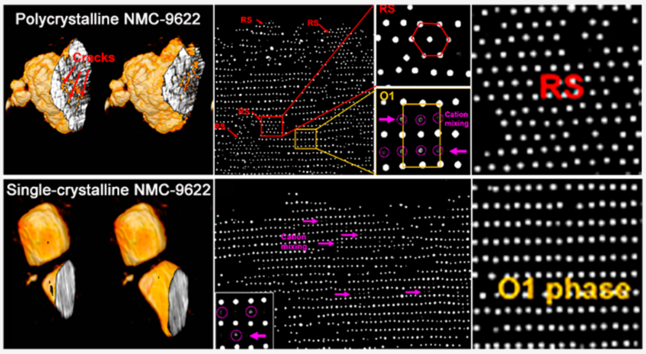

ABSTRACT: The pressing demand in electrical vehicle (EV) markets for high-energy-density lithium-ion batteries (LIBs) requires further increasing the Ni content in high-Ni and low-Co cathodes. However, the commercialization of high-Ni cathodes is hindered by their intrinsic chemomechanical instabilities and fast capacity fade. The emerging single-crystalline strategy offers a promising solution, yet the operation and degradation mechanism of single-crystalline cathodes remain elusive, especially in the extremely challenging ultrahigh-Ni (Ni > 90%) regime whereby the phase transformation, oxygen loss, and mechanical instability are exacerbated with increased Ni content. Herein, we decipher the atomic-scale stabilization mechanism controlling the enhanced cycling performance of an ultrahigh-Ni single-crystalline cathode. We find that the charge/discharge inhomogeneity, the intergranular cracking, and oxygen-loss-related phase degradations that are prominent in ultrahigh-Ni polycrystalline cathodes are considerably suppressed in their single-crystalline counterparts, leading to improved chemomechanical and cycling stabilities of the single-crystalline cathodes. Our work offers important guidance for designing next-generation single-crystalline cathodes for high-capacity, long-life LIBs.

KEYWORDS: *single-crystalline, cathodes, lithium-ion batteries, ultrahigh Ni, chemomechanical, degradation*

High-Ni-content layered cathodes, because of their high theoretical specific capacity, are considered to be an ultimate choice for high-energy-density automotive batteries.[1−5] However, conventional polycrystalline high-Ni-content layered oxides suffer from fast capacity fade due to severe structural/chemomechanical instabilities[6−8] and oxygen-loss[9,10] induced phase degradations.[11] The culprits of high-Ni-content cathodes are closely related to its widely adopted primary−secondary particle architecture. Layered oxide cathodes are usually synthesized in the form of secondary particles (~5−30 μm in size) comprising densely packed primary particles (~50−300 nm in size). The use of secondary particles increases the tapping density and thereby slows the cathode side reactions/corrosions to some extent;[12] however, it also introduces drawbacks, among which intergranular cracking, i.e., cracking along boundaries of primary particles is a major cause of layered cathodes' long-cycle capacity fading.[13] Distinct from the grain boundaries in polycrystalline metals or ceramics which are covalently bonded, primary particles are held together mainly by weak van der Waals interactions.[14] That is to say, secondary particles' mechanical strength, determined by the adhesion of the constituent primary particles, is much lower than the intrinsic material strength of the single-crystalline primary particles. As a result, intergranular cracking and related electro-chemomechanical degradation in secondary particles can be easily induced under the anisotropic stress and strain generated by Li extraction and insertion.[15] As these cracks create fresh surfaces to electrolytes, the breakdown of the cathodes will be exacerbated by side reactions, oxygen loss, and detrimental phase degradations.[16,17] The ever-increasing Ni content in the cathodes driven by the urgent demand to reduce the cobalt content and achieve higher energy density for electric vehicle applications makes the situation worse. A prevalent strategy to resolve the cycling instability associated with the structural instability of the high-Ni-content cathode is cationic doping. Intensive experimental works reported that single-element doping, such as Al,[18] Mg,[19] Ti,[20] Sb,[21] Ca,[22] W,[23] and Zr,[24] shows different degrees of improvement in terms of layered cathodes' cycling stability. Also, dual-element doping such as Mg/Ti[25] and Mg/Mn[26] have been proved effective in improving the rate capability,

Received: October 5, 2021
Revised: November 4, 2021

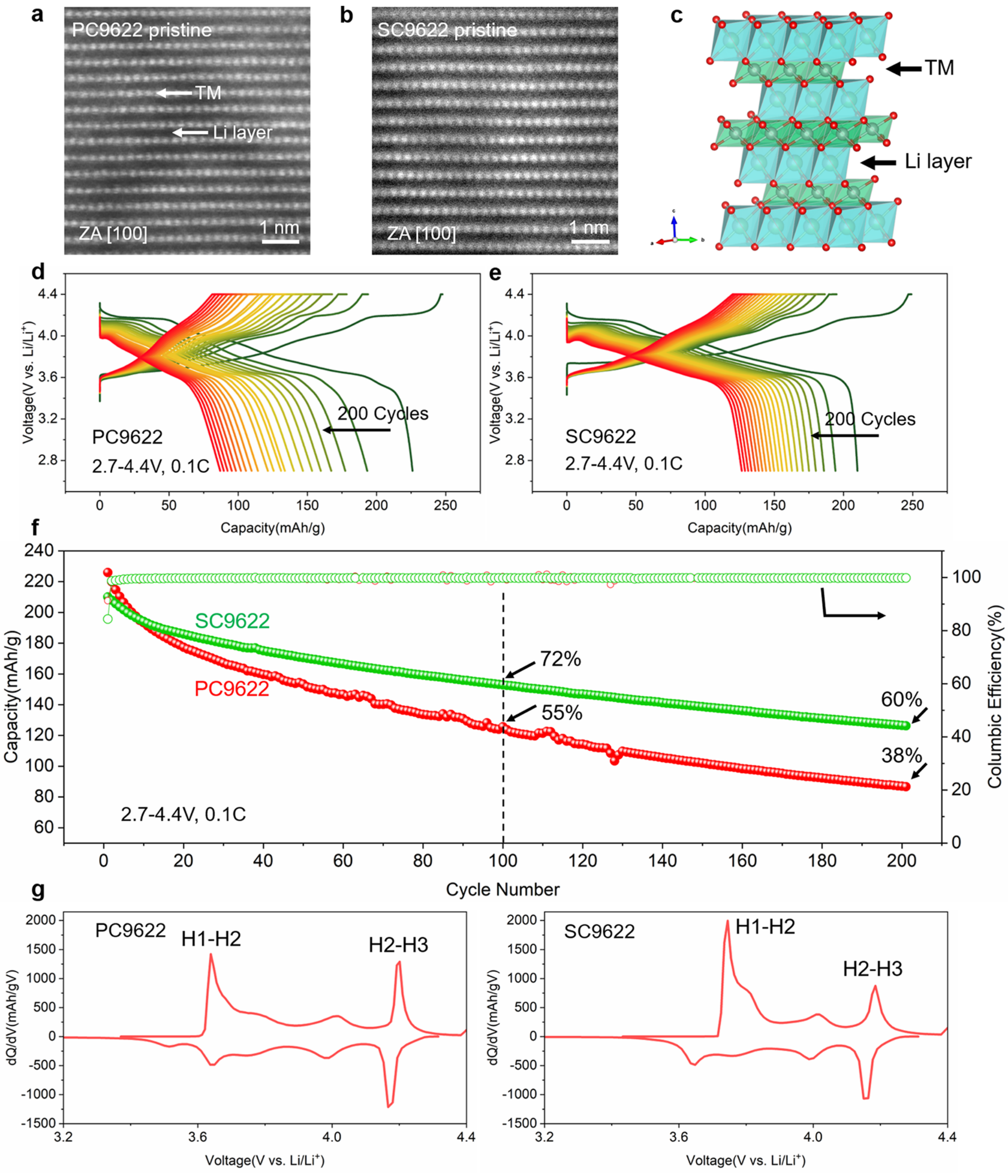

Figure 1. (a, b) High-angle annular dark-field scanning transmission electron microscopy (HAADF-STEM) images of SC9622 and PC9622 ultrahigh-Ni cathodes. Both cathodes show a perfect layered structure with a space group of $R\bar{3}m$. (c) Atomic models of the layered structure of the cathodes. (d) Long-cycle charge−discharge profiles of coin cells containing PC9622 within 2.7−4.4 V at the current of 0.1C. (e) Long-cycle charge−discharge profiles of coin cells containing SC9622 within 2.7−4.4 V at the current of 0.1C. (f) Capacity retentions and Columbic efficiencies (CEs) of SC9622 and PC9622 during long-term cycling. (g) dQ/dV curves showing the H1−H2 and H2−H3 phase transitions in PC9622 and SC9622.

thermal stability, and self-discharge resistance of $LiNiO_2$, yet the structural instability and fast capacity decay problem of high-Ni and especially ultrahigh-Ni cathodes are still far from well resolved. In this context, fabricating micrometer-sized large single-crystalline cathode particles that evade the traditional primary−secondary particle architecture provides a promising solution to overcome the cycling instability issues of existing Ni-rich cathodes.[13,27−33] For example, for Ni-rich cathodes with relatively low Ni content,[28,32] the single-crystalline strategy significantly improves the cathodes' cycling stability almost without sacrificing their initial capacity. Most recently, Xiao and co-workers[13] reported a novel single-crystalline $LiNi_{0.76}Mn_{0.14}Co_{0.1}O_2$ cathode with improved stability through reversible microcracking. These studies aroused tremendous research interests in the community as they open a new avenue to optimizing Ni-rich cathodes. To date, in the ongoing pursuit of further increasing the Ni content in current layered cathodes, it is not clear how the single-crystalline strategy performs when entering the extremely challenging ultrahigh-Ni (Ni > 90%) regime. Particularly, considering the delithiation-induced O1 phase transformation[16] and oxygen loss[6] dramatically increase with the Ni content in conventional polycrystalline cathodes, how these degradation modes operate in ultrahigh-Ni single-crystalline cathodes remains unclear. Here, we report the first high-capacity single-crystalline layered cathode ($Li-Ni_{0.96}Co_{0.02}Mn_{0.02}O_2$) with Ni content up to 96%, and using it as a ultrahigh-Ni model system, we uncover the fundamental

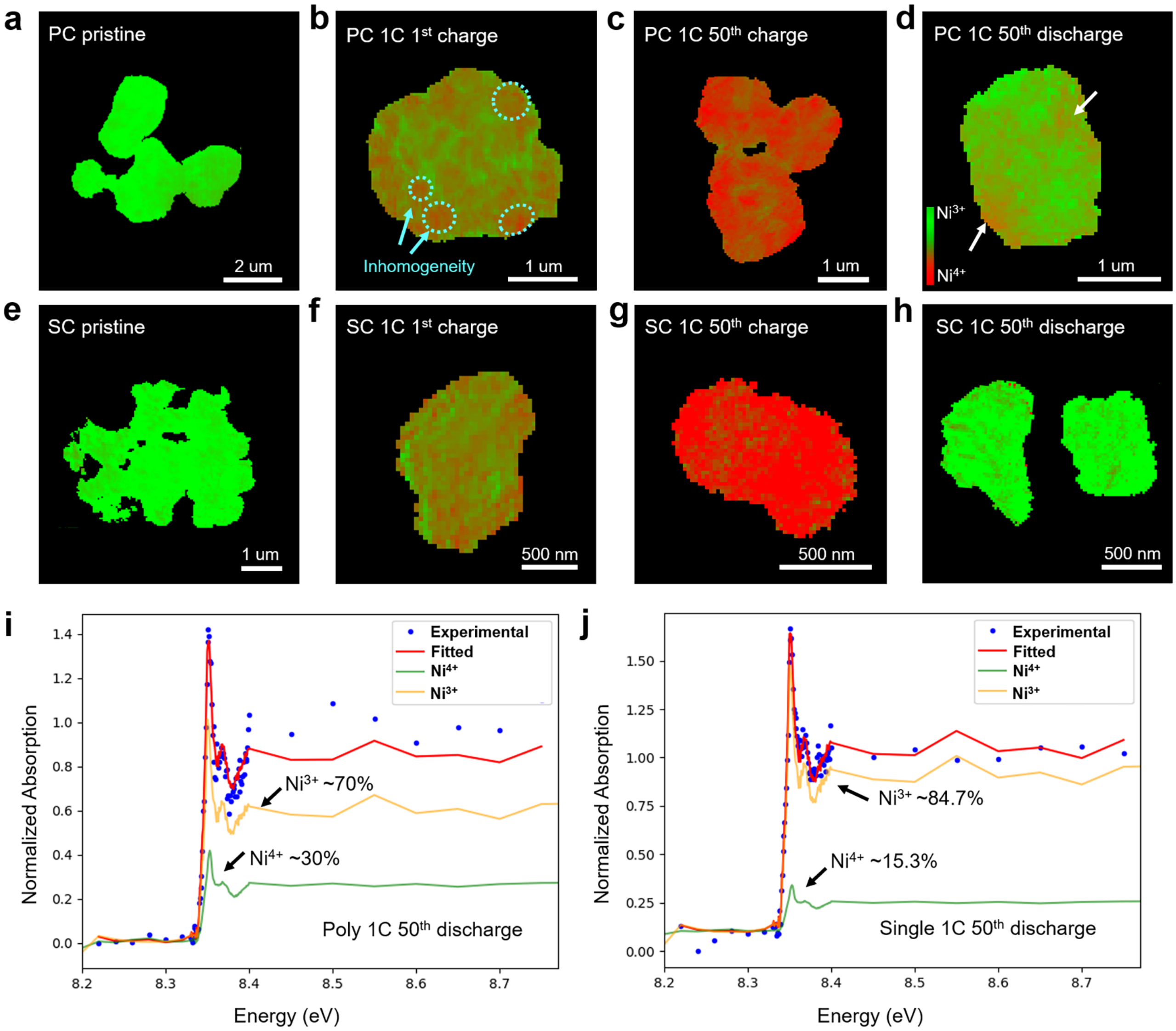

Figure 2. (a–d) Ni^{3+} and Ni^{4+} distributions in pristine PC9622 and those after the 1st charge, 50th charge, and 50th discharge. Charge and discharge inhomogeneities are identified in the secondary particles. (e–h) Ni^{3+} and Ni^{4+} distributions in pristine SC9622 and those after the 1st charge, 50th charge, and 50th discharge. Fewer charge and discharge inhomogeneities are observed in SC9622 compared with PC9622. (i) Quantification of the Ni^{3+} and Ni^{4+} in the 50th discharged PC9622 cathode. (j) Quantification of the Ni^{3+} and Ni^{4+} in the 50th discharged SC9622 cathode. The higher percentage of Ni^{4+} in the long-cycle discharged PC9622 indicates that fewer Li^+ are intercalated back into the cycled PC9622 lattice than in SC9622, suggesting superior structural stability and capacity retention of the SC9622 cathode over the PC9622 cathode.

mechanisms that underpin the improved cycling stability of a single-crystalline cathode over its polycrystalline counterpart. By combining multiple techniques including X-ray absorption spectroscopy (XAS), transmission X-ray microscopy (TXM) tomography, and atomic-resolution imaging, we find that the prominent charge/discharge inhomogeneity, the internal strain-induced cracks, and the severe oxygen-loss induced rock salt (RS) phase degradation are effectively mitigated by the single-crystalline strategy.

In this work, a novel single-crystalline ultrahigh-Ni layered cathode with a designed composition of $LiNi_{0.96}Mn_{0.02}Co_{0.02}O_2$ (hereafter referred to as SC9622) was synthesized (see SEM images of the precursors and as-prepared SC9622 cathodes in Figure S1 and details in Experimental Methods). A baseline polycrystalline cathode with the same designed composition (hereafter referred to as PC9622) was also synthesized for comparative studies (see SEM images of the precursors and as-prepared PC9622 cathodes in Figure S2). X-ray diffractions (Figure S3) show that both cathodes have nearly the same lattice structure and chemical analysis (Figure S4) shows that both synthesized cathodes have similar compositions nearly the same as the designed compositions. Figure 1a ,b shows the high-angle annular dark-field scanning transmission electron microscopy (HAADF-STEM) images of PC9622 and SC9622 cathodes. The results, along with the electron diffractions (Figure S5) show that both pristine cathodes have a well-defined layered structure (space group: $R\bar{3}m$) as illustrated by the atomic model in Figure 1c. Electrochemical tests were conducted to evaluate the performance of SC9622 in comparison with PC9622. Figure 1d, e shows the charge–discharge profiles of SC9622 and PC9622, respectively. The results show that the PC9622 delivers an initial discharge capacity of ~225 mAh/g (within 2.7–4.4 V at a 0.1C rate), whereas SC9622 delivers a slightly lower initial discharge

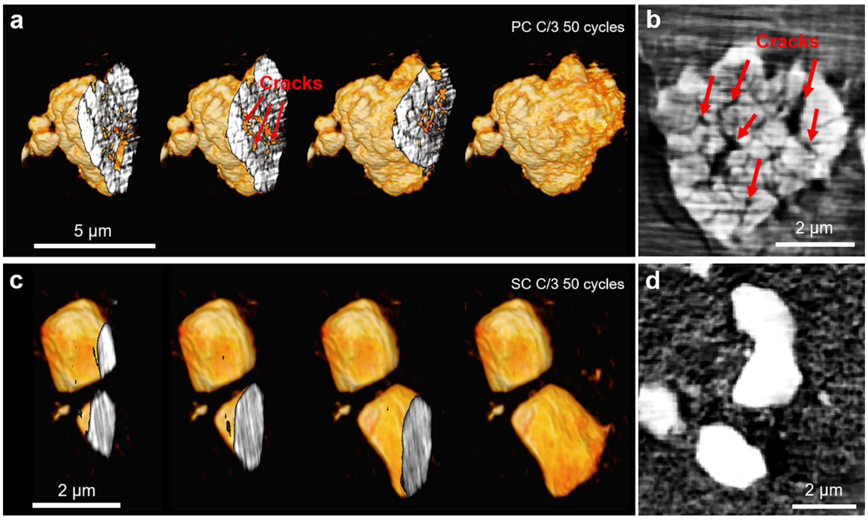

Figure 3. (a) 3D tomographic reconstruction and multislicing analysis of a representative PC9622 secondary particle after long-term cycling. Intergranular cracks are identified in the particle. (b) Cross-section image of another cracked PC9622 secondary particle after cycling. Some of the cracks are indicated by the arrows. (c) 3D tomographic reconstruction and multislicing analysis of representative SC9622 particles after long-term cycling. Cracks are not observed inside the particles. (d) Cross-section image showing intact SC9622 particles after cycling.

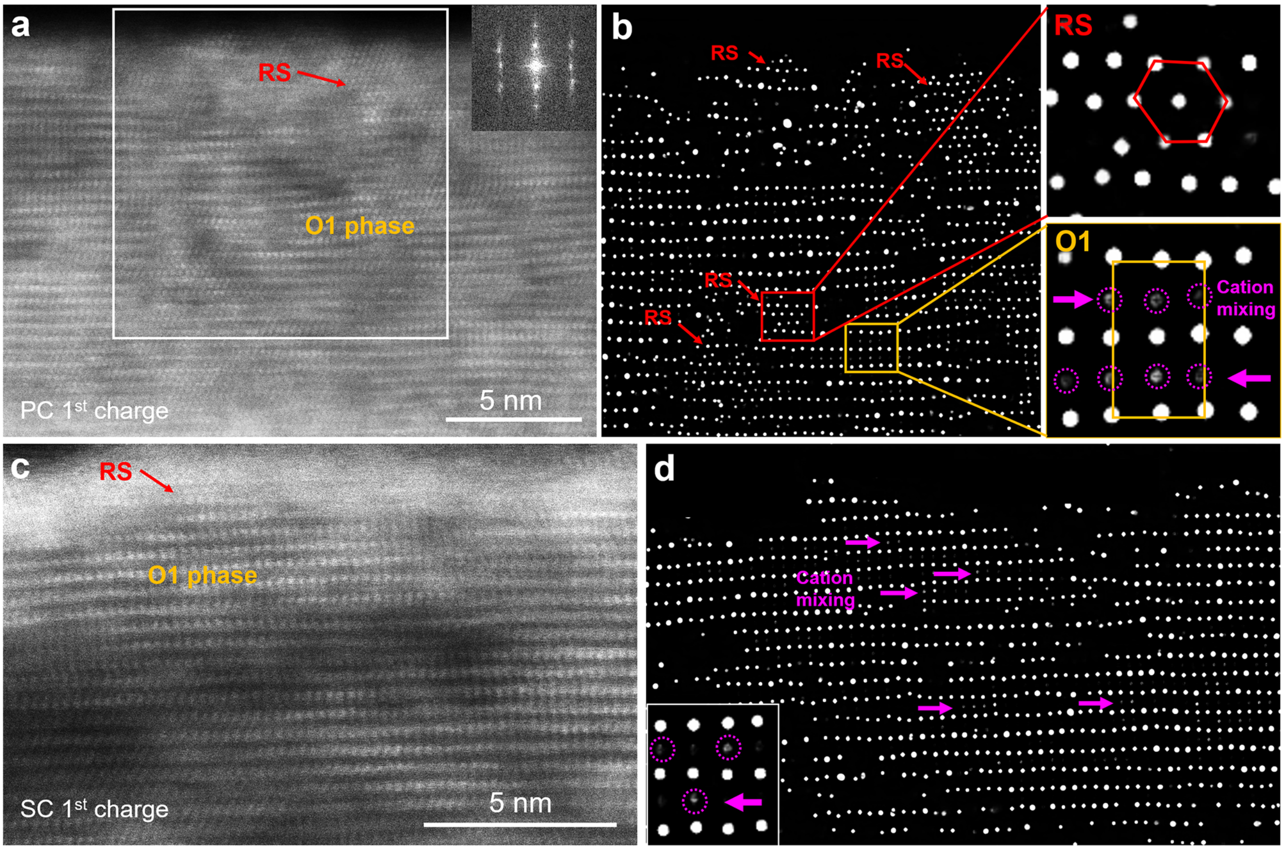

Figure 4. (a) Atomic-resolution HAADF-STEM image of a 1st charged PC9622 cathode taken along the [100] zone axis. (b) Super-resolution image corresponding to the boxed region in panel a obtained by *AtomSegNet*.[36] The result shows that the O1 phase forms substantially on the surface of the particle. Because of local cation mixing, local rocksalt (RS) domains (indicated by arrows) are identified in the bulk O1 phase, especially close to the particle surface. The insets highlight an RS domain and an O1 block with cation mixing (TM atomic columns are denoted by dash circles) in the buck O1 phase. (c) Atomic-resolution HAADF-STEM image of a 1st charged SC9622 cathode taken along the [100] zone axis. (d) Super-resolution image derived from the HAADF-STEM image in panel c. Bulk O1 phase and local cation mixing (highlighted by the dash circles in the inset) similar to that in PC9622 are also identified in SC9622. Note that except for a small amount of RS at the surface as indicated by the arrow in panel c, local RS domains are not formed in the bulk O1 phase.

capacity of ~210 mAh/g at the same condition. Long-term cycling tests (Figure 1f) show that the capacity of PC9622 suffers from severe decay as the capacity retention rapidly drops to as low as ~55% after 100 cycles and 38.3% after 200

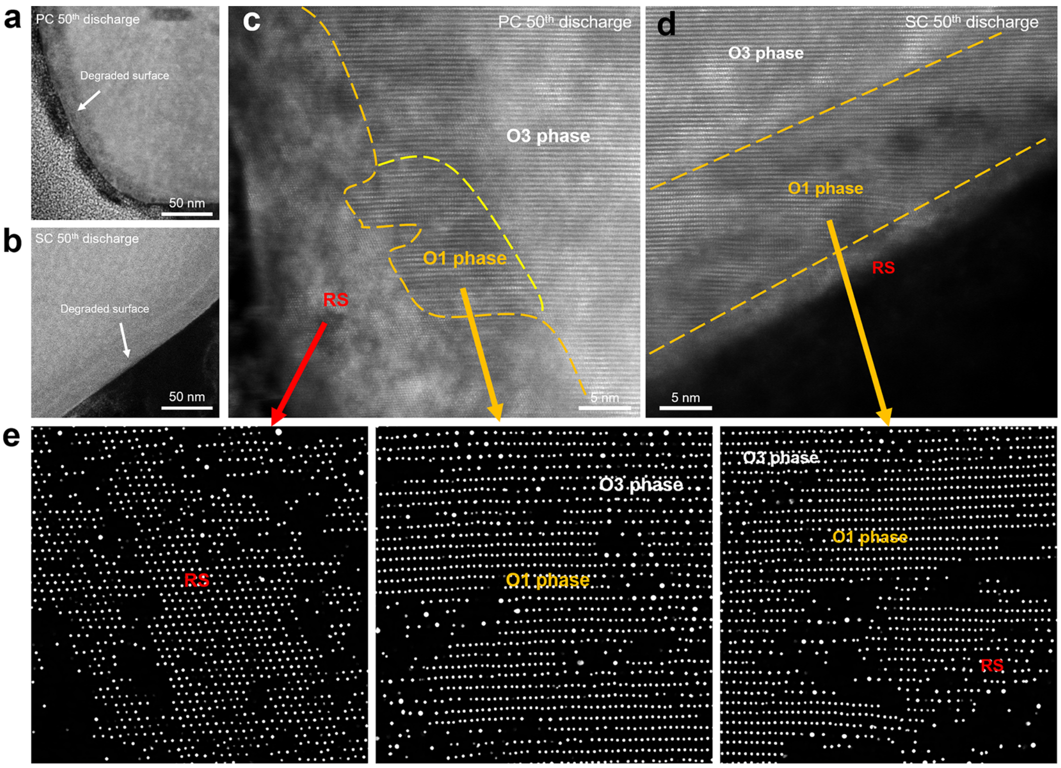

Figure 5. (a, b) HAADF-STEM images showing the morphology of long-term cycled PC9622 primary particle and SC9622 particle (the degraded surface layers are indicated by the arrows). (c, d) Atomic-resolution HAADF-STEM images showing the structures of cycled PC9622 and SC9622 cathodes. (e) Super-resolution images derived from the HAADF-STEM images in panels c and d by *AtomSegNet* processing. The results show that after long-term cycling, a thick RS layer (~20−30 nm thick) forms on the surface of the PC9622 particle. A residual O1 phase existing between the surface RS and the interior O3 phase is also observed. In contrast, only a thin layer of RS phase (not effectively determined by *AtomSegNet* because of the low contrast resulted from its small thickness) is identified in panel d at the surface of the SC9622 particle and the subsurface degradation layer still largely remains as O1 phase.

cycles; in contrast, the capacity retention of SC9622 is ~72% after 100 cycles and ~60% after 200 cycles, which is remarkably improved compared to that of PC9622. The dQ/dV profiles (Figure 1g) of both cathodes show that although the H1−H2 phase transition is more evident in SC9622, the more detrimental H2−H3 transition is considerably suppressed, as indicated by the flattened peak at the same voltage.

TXM X-ray absorption near-edge spectroscopic (XANES) imaging[34] was performed to elucidate the changing Ni valence states of SC9622 and PC9622 upon cycling. Figure 2 shows the Ni valence state maps (Ni^{3+} and Ni^{4+}) of both cathodes and their evolution at different states. The pristine and 0.1C fully charged PC9622 are used as references (Figure S6). It is seen that the 1st charged PC9622 (Figure 2b) show inhomogeneous Ni valence distributions (Ni^{4+} blocks are indicated by dashed circles) with a length scale of ~200−500 nm, which is comparable to the grain size of the PC9622 primary particles. In contrast, although the Ni valence distributions in the 1st charged SC9622 (Figure 2f) also show inhomogeneity similar to that in single-crystalline cathode with relatively low Ni content,[35] the length scale of the Ni^{4+} blocks is around 100 nm, much smaller than that in their polycrystalline counterpart. The alleviated charge inhomogeneity in the single-crystalline cathode is likely attributed to the elimination of the differently oriented grain boundaries that impede the homogeneous diffusion of Li^+ in the secondary particles and to the varied surface RS phase transformation in different primary particles. Figure 2c, g shows the Ni valence state maps of SC9622 and PC9622 charged particles after long cycles. The results show that the severe charge/discharge inhomogeneity in PC9622 persists after long cycles (Figure 2c, d), whereas SC9622 shows charge/discharge inhomogeneity with a much smaller length scale (Figure 2g, h). By quantifying the Ni valence state in the long-cycle discharged cathodes, we find that the percentage of Ni^{4+} in PC9622 cathode is evidently higher than that in SC9622 cathode (Figure 2i,j), suggesting that fewer Li^+ are intercalated back into the cycled PC9622 lattice than that in SC9622. This agrees well with the fast capacity decay of PC9622 cathode revealed in the electrochemical tests in Figure 1f.

TXM tomographic imaging, a three-dimensional (3D) imaging technique, was performed to evaluate the chemomechanical stability of SC9622 cathode in comparison with PC9622. Figure 3 shows representative 3D tomographic reconstructions of long-term cycled PC9622 and SC9622 cathodes. Multislicing analyses of the reconstructions show that after long-term cycling, substantial intergranular cracks formed inside the PC9622 secondary particles (Figure 3a). Figure 3b shows a cross-section image of another PC9622 particle inside which multiple cracks (indicated by the arrows) are identified. In sharp contrast, The long-term cycled SC9622 remains intact after long cycles as revealed by the 3D reconstruction (Figure 3c) and cross-section image (Figure 3d). These results reveal the superior chemomechanical stability of the single-crystalline SC9622 cathodes over their polycrystalline counterparts.

Comprehensive atomic-scale TEM imaging was performed to study the structural stability and degradation pathways of both cathodes comparatively. Usually, for LIB cathode materials, especially the highly unstable delithiated phases which are very beam-sensitive, the relatively low electron dose used for the atomic-resolution imaging easily leads to a poor signal-to-noise ratio which may bury the atomic details (e.g., trace amount of TM atoms in Li layers) of the materials. Therefore, a robust strategy to detect atomic columns and restore the in-depth information hidden behind the nonideal atomic-resolution images is highly desirable. In this work, to precisely decipher the atomic structural information hidden in the original HAADF-STEM images with complex contrast, a deep-learning-based *AtomSegNet*[36] software was employed to perform atomic column localization and segmentation (see details in the Supporting Information). Figure 4a shows a representative HADDF-STEM image of 1st charged PC9622 cathode at a cutoff voltage of 4.4 V. It is seen that during delithiation, a substantial amount of O1 phase formed near the particle's surface. Moreover, because of surface oxygen loss, a layer of RS phase was formed on top of the bulk O1 phase. The super-resolution image (Figure 4b) of the boxed region in Figure 4a shows that local RS transformations (RS domains indicated by the arrows in Figure 4b) already took place inside the bulk O1 phase. The upper right panel highlights an RS block (corresponding to the red boxed region) embedded in the bulk O1 phase. Moreover, cation mixing, i.e. migration of TM atoms from TM layer to Li sites are detected in local regions (lower right panel of Figure 4b, corresponding to the orange boxed region in the left panel) of the bulk O1 phase. The relatively weak contrast of the TM atomic columns (indicated by the magenta circles) in the Li layers suggests that the cation mixing, although detrimental, is not yet sufficient to trigger the transformation from the O1 phase to RS which requires further interlayer gliding between the TM layers in the O1 lattice (see ref 6 for a detailed discussion on this newly discovered phase transformation pathway). Figures 4c shows a representative HAADF-STEM image of 1st charged SC9622 at a cutoff voltage of 4.4 V. Similar to that in PC9622 cathode, bulk O1 phase also formed near the particle's surface. Although a thin layer of RS phase also formed on the top of the O1 phase, no RS domains were observed inside the bulk O1 phase, indicating there is less severe oxygen loss in the O1 phase of SC9622. The super-resolution image (corresponding to the image in Figure 4c) in Figure 4d shows that cation mixing (TM atomic columns indicated by magenta circles) also took place in local regions of the O1 phase, yet the intensities of these cations are weak and their distribution is more dispersive than that in the bulk O1 phase of the PC9622 cathode. This implies that the oxygen loss on the surface of the SC9622 cathode is relatively weaker and more uniform than that in PC9622, which is consistent with the trend revealed in the XANES maps in Figure 2b, f.

To elucidate the structural degradation pathways of SC9622 during long-term cycling, we further investigate its structural evolution in comparison with that of PC9622. Figure 5a, b shows representative morphologies of a PC9622 and SC9622 particle after long-term cycling (50 cycles at a 1C rate). It is seen that for both cathodes, surface degradation layers (∼20–30 nm in thickness) were observed. Atomic-resolution HAADF-STEM imaging results (Figure 5c and the magnified super-resolution images in Figure 5e) reveal that the degraded surface layer is composed of a significantly thickened outer layer of RS and inner O1 phase blocks. This suggests that, after long cycles, a large proportion of the bulk O1 phase which is preferentially formed on the surface of PC9622 finally transformed into inactive RS. In contrast, for the long-term cycled SC9622 cathode (Figure 5d and the magnified super-resolution image in Figure 5e), although an RS layer also formed on the outer surface, a large proportion of the degraded surface layer (inner layer) remained as bulk O1 phase. Although the surface RS layer of SC9622 cathode was thickened compared with that in the first cycle (Figure 4c), it is considerably thinner than that in the long-term cycled PC9622 cathode (Figure 5c), suggesting that the oxygen loss and thereby the surface RS transformation in SC9622 is significantly mitigated compared with that in PC9622 cathode. The observations elucidate, at the atomic scale, the origin of the remarkably improved capacity retention of SC9622 compared with that of the PC9622 cathode.

The key difference between the SC cathodes and their PC counterparts lies in (1) the reduced surface to volume ratio and (2) the loss of the conventional secondary-particle architecture in SC cathodes. First, the decreased surface area of the SC cathodes originating from the increased average particle size (compared to the primary particles of PC cathodes) is responsible for the lower initial capacity of the SC cathodes. This is because, for a certain system with fixed chemical composition, larger particles have longer Li^+ diffusion lengths[13] and smaller total surface area, which leads to a decreased reaction area with electrolytes. Despite that, the benefit of the reduced electrolyte exposure is that it alleviates the side reactions that promote surface oxygen loss[6] and thereby mitigate the RS degradations[11] to some extent. On the other hand, because the conventional secondary particles of PC cathodes are formed by dozens or hundreds of agglomerated primary particles with different crystallographic orientations, charge inhomogeneity (e.g., Figure 2b) is inevitable in these closely packed primary particles (Li^+ diffusion along the (003) planes of the layered lattice is energetically favorable). The inhomogeneous Li^+ diffusion kinetics unavoidably causes a severely nonuniform volume change and local strain[4] in the secondary particles at a high state-of-charge and finally results in intergranular cracks[37,38] and even pulverization of the PC cathodes. As the intergranular cracking exposes new surfaces to the electrolyte for side reactions, the degradation of the cathode will be accelerated.[39] In contrast, by eliminating the secondary-particle architecture, the micrometer-sized SC particles are relatively loosely aggregated, and thus the intergranular cracking caused by local stress generation between cathode particles can be effectively mitigated.

In conclusion, through combined synchrotron-based transmission X-ray techniques and atomic-resolution STEM imaging, we decipher the atomic-scale stabilization mechanism underneath the enhanced cycling performance of an ultrahigh-Ni single-crystalline cathode. We uncover that the charge/discharge inhomogeneity as well as oxygen-loss-related phase degradations that are prominent in ultrahigh-Ni polycrystalline cathodes are considerably suppressed in their single-crystalline counterpart, leading to the improved cycling stability of the single-crystalline cathode. The new understanding of the degradation pathways of the ultrahigh-Ni single-crystalline cathode is expected to be applicable to other high-Ni single-crystalline layered cathodes, and it will offer valuable guidance for the optimization and redesign of current ultrahigh-Ni cathodes for ultrastable and long-life batteries.

■ ASSOCIATED CONTENT

Supporting Information

The Supporting Information is available free of charge at https://pubs.acs.org/doi/10.1021/acs.nanolett.1c03852.

> Materials and methods, SEM images of SC9622 and PC9622 precursors and cathodes, XRD of SC9622 and PC9622 cathodes, EDS analysis, electron diffraction patterns, and XANES reference spectra (PDF)

■ AUTHOR INFORMATION

Corresponding Authors

Youngho Shin − *Materials Engineering Research Facility, Applied Materials Division, Argonne National Laboratory, Lemont, Illinois 60439, United States*; Email: yshin@anl.gov

Huolin L. Xin − *Department of Physics and Astronomy, University of California, Irvine, California 92697, United States*; orcid.org/0000-0002-6521-868X; Email: huolinx@uci.edu

Authors

Chunyang Wang − *Department of Physics and Astronomy, University of California, Irvine, California 92697, United States*; orcid.org/0000-0001-8461-3952

Rui Zhang − *Department of Physics and Astronomy, University of California, Irvine, California 92697, United States*

Carrie Siu − *Materials Engineering Research Facility, Applied Materials Division, Argonne National Laboratory, Lemont, Illinois 60439, United States*

Mingyuan Ge − *National Synchrotron Light Source II, Brookhaven National Laboratory, Upton, New York 11973, United States*

Kim Kisslinger − *Center for Functional Nanomaterials, Brookhaven National Laboratory, Upton, New York 11973, United States*

Complete contact information is available at: https://pubs.acs.org/10.1021/acs.nanolett.1c03852

Author Contributions

H.L.X. and Y.S. conceived and directed the project. Y.S. and C.S. performed materials synthesis and electrochemical evaluations. C.Y.W. performed the TEM experiments and data analysis. R.Z. performed electrochemical cycling of the materials for microscopy studies. C.Y.W., R.Z., and M.Y.G. performed TXM tomography and XANES experiments and data analysis. K.K. prepared the TEM samples. C.Y.W. and H.L.X. wrote the paper with help of all authors.

Notes

The authors declare no competing financial interest.

■ ACKNOWLEDGMENTS

This work is supported by the U.S. Department of Energy (DOE) Office of Energy Efficiency and Renewable Energy under award DEEE0008444. The TEM and deep-learning assistant imaging are supported by the Early Career Research Program, Materials Science and Engineering Divisions, Office of Basic Energy Sciences of the U.S. Department of Energy, under award DE-SC0021204. R.Z.'s work done for this study was funded by H.L.X.'s startup funding. This research used resources of the Center for Functional Nanomaterials and the 18-ID (FXI) beamline of the National Synchrotron Light Source II, which are U.S. DOE Office of Science Facilities, at Brookhaven National Laboratory under contract DESC0012704. This work was partially carried out at the MERF facility, which is supported within the core funding of the Applied Battery Research for Transportation Program. We gratefully acknowledge the support from the U.S. Department of Energy, Office of Vehicle Technologies, particularly from Peter Faguy and Dave Howell. The submitted manuscript has been created by UChicago Argonne, LLC, Operator of Argonne National Laboratory ("Argonne"). Argonne, a U.S. Department of Energy Office of Science laboratory, is operated under Contract DE-AC02-06CH11357. The U.S. Government retains for itself, and others acting on its behalf, a paid-up nonexclusive, irrevocable worldwide license in said article to reproduce, prepare derivative works, distribute copies to the public, and perform publicly and display publicly, by or on behalf of the government.

■ REFERENCES

(1) Li, W.; Erickson, E. M.; Manthiram, A. High-nickel layered oxide cathodes for lithium-based automotive batteries. *Nature Energy* **2020**, *5*, 26−34.

(2) Liu, T.; Yu, L.; Liu, J.; Lu, J.; Bi, X.; Dai, A.; Li, M.; Li, M.; Hu, Z.; Ma, L.; Luo, D.; Zheng, J.; Wu, T.; Ren, Y.; Wen, J.; Pan, F.; Amine, K. Understanding Co roles towards developing Co-free Ni-rich cathodes for rechargeable batteries. *Nature Energy* **2021**, *6*, 277.

(3) Lin, R.; Bak, S. M.; Shin, Y.; Zhang, R.; Wang, C.; Kisslinger, K.; Ge, M.; Huang, X.; Shadike, Z.; Pattammattel, A.; et al. Hierarchical nickel valence gradient stabilizes high-nickel content layered cathode materials. *Nat. Commun.* **2021**, *12* (1), 2350.

(4) Voronina, N.; Sun, Y.-K.; Myung, S.-T. Co-Free Layered Cathode Materials for High Energy Density Lithium-Ion Batteries. *ACS Energy Letters* **2020**, *5* (6), 1814−1824.

(5) Li, W.; Lee, S.; Manthiram, A. High-Nickel NMA: A Cobalt-Free Alternative to NMC and NCA Cathodes for Lithium-Ion Batteries. *Adv. Mater.* **2020**, 32 (33), 2002718.

(6) Wang, C.; Han, L.; Zhang, R.; Cheng, H.; Mu, L.; Kisslinger, K.; Zou, P.; Ren, Y.; Cao, P.; Lin, F.; Xin, H. L. Resolving atomic-scale phase transformation and oxygen loss mechanism in ultrahigh-nickel layered cathodes for cobalt-free lithium-ion batteries. *Matter* **2021**, *4* (6), 2013−2026.

(7) Yan, P.; Zheng, J.; Chen, T.; Luo, L.; Jiang, Y.; Wang, K.; Sui, M.; Zhang, J. G.; Zhang, S.; Wang, C. Coupling of electrochemically triggered thermal and mechanical effects to aggravate failure in a layered cathode. *Nat. Commun.* **2018**, *9* (1), 2437.

(8) Lin, R.; Hu, E.; Liu, M.; Wang, Y.; Cheng, H.; Wu, J.; Zheng, J.-C.; Wu, Q.; Bak, S.; Tong, X.; et al. Anomalous metal segregation in lithium-rich material provides design rules for stable cathode in lithium-ion battery. *Nat. Commun.* **2019**, *10* (1), 1650.

(9) Yan, P.; Zheng, J.; Tang, Z. K.; Devaraj, A.; Chen, G.; Amine, K.; Zhang, J. G.; Liu, L. M.; Wang, C. Injection of oxygen vacancies in the bulk lattice of layered cathodes. *Nat. Nanotechnol.* **2019**, *14* (6), 602−608.

(10) Cheng, J.; Mu, L.; Wang, C.; Yang, Z.; Xin, H. L.; Lin, F.; Persson, K. A. Enhancing surface oxygen retention through theory-guided doping selection in Li1−xNiO2 for next-generation lithium-ion batteries. *J. Mater. Chem. A* **2020**, *8* (44), 23293−23303.

(11) Lin, F.; Markus, I. M.; Nordlund, D.; Weng, T. C.; Asta, M. D.; Xin, H. L.; Doeff, M. M. Surface reconstruction and chemical evolution of stoichiometric layered cathode materials for lithium-ion batteries. *Nat. Commun.* **2014**, *5* (1), 3529.

(12) Yan, P.; Zheng, J.; Gu, M.; Xiao, J.; Zhang, J.-G.; Wang, C.-M. Intragranular cracking as a critical barrier for high-voltage usage of

layer-structured cathode for lithium-ion batteries. *Nat. Commun.* **2017**, *8*, 14101.

(13) Bi, Y.; Tao, J.; Wu, Y.; Li, L.; Xu, Y.; Hu, E.; Wu, B.; Hu, J.; Wang, C.; Zhang, J.-G.; Qi, Y.; Xiao, J. Reversible planar gliding and microcracking in a single-crystalline Ni-rich cathode. *Science* **2020**, *370* (6522), 1313−1317.

(14) Xu, R.; de Vasconcelos, L. S.; Shi, J.; Li, J.; Zhao, K. Disintegration of Meatball Electrodes for LiNi x Mn y Co z O2 Cathode Materials. *Exp. Mech.* **2018**, *58* (4), 549−559.

(15) Mu, L.; Lin, R.; Xu, R.; Han, L.; Xia, S.; Sokaras, D.; Steiner, J. D.; Weng, T.-C.; Nordlund, D.; Doeff, M. M.; Liu, Y.; Zhao, K.; Xin, H. L.; Lin, F. Oxygen Release Induced Chemomechanical Breakdown of Layered Cathode Materials. *Nano Lett.* **2018**, *18* (5), 3241−3249.

(16) Wang, C.; Zhang, R.; Kisslinger, K.; Xin, H. L. Atomic-Scale Observation of O1 Faulted Phase-Induced Deactivation of LiNiO2 at High Voltage. *Nano Lett.* **2021**, *21* (8), 3657−3663.

(17) Zhang, H.; Omenya, F.; Yan, P.; Luo, L.; Whittingham, M. S.; Wang, C.; Zhou, G. Rock-Salt Growth-Induced (003) Cracking in a Layered Positive Electrode for Li-Ion Batteries. *ACS Energy Letters* **2017**, *2* (11), 2607−2615.

(18) Gupta, A.; Chemelewski, W. D.; Buddie Mullins, C.; Goodenough, J. B. High-Rate Oxygen Evolution Reaction on Al-Doped LiNiO2. *Adv. Mater.* **2015**, *27* (39), 6063−6067.

(19) Muto, S.; Tatsumi, K.; Kojima, Y.; Oka, H.; Kondo, H.; Horibuchi, K.; Ukyo, Y. Effect of Mg-doping on the degradation of LiNiO2-based cathode materials by combined spectroscopic methods. *J. Power Sources* **2012**, *205*, 449−455.

(20) Kwon, S. N.; Park, H. R.; Song, M. Y. Electrochemical performances of LiNiO2 substituted by Ti for Ni via the combustion method. *Ceram. Int.* **2014**, *40* (7), 11131−11137.

(21) Cui, P.; Jia, Z.; Li, L.; He, T. Preparation and characteristics of Sb-doped LiNiO2 cathode materials for Li-ion batteries. *J. Phys. Chem. Solids* **2011**, *72* (7), 899−903.

(22) Chen, M.; Zhao, E.; Chen, D.; Wu, M.; Han, S.; Huang, Q.; Yang, L.; Xiao, X.; Hu, Z. Decreasing Li/Ni disorder and improving the electrochemical performances of Ni-rich LiNi0. 8Co0. 1Mn0. 1O2 by Ca doping. *Inorg. Chem.* **2017**, *56* (14), 8355−8362.

(23) Ryu, H.-H.; Park, G.-T.; Yoon, C. S.; Sun, Y.-K. Suppressing detrimental phase transitions via tungsten doping of LiNiO 2 cathode for next-generation lithium-ion batteries. *J. Mater. Chem. A* **2019**, *7* (31), 18580−18588.

(24) Yoon, C. S.; Kim, U.-H.; Park, G.-T.; Kim, S. J.; Kim, K.-H.; Kim, J.; Sun, Y.-K. Self-Passivation of a LiNiO2 Cathode for a Lithium-Ion Battery through Zr Doping. *ACS Energy Letters* **2018**, *3* (7), 1634−1639.

(25) Mu, L.; Zhang, R.; Kan, W. H.; Zhang, Y.; Li, L.; Kuai, C.; Zydlewski, B.; Rahman, M. M.; Sun, C.-J.; Sainio, S.; Avdeev, M.; Nordlund, D.; Xin, H. L.; Lin, F. Dopant Distribution in Co-Free High-Energy Layered Cathode Materials. *Chem. Mater.* **2019**, *31* (23), 9769−9776.

(26) Mu, L.; Kan, W. H.; Kuai, C.; Yang, Z.; Li, L.; Sun, C. J.; Sainio, S.; Avdeev, M.; Nordlund, D.; Lin, F. Structural and Electrochemical Impacts of Mg/Mn Dual Dopants on the LiNiO2 Cathode in Li-Metal Batteries. *ACS Appl. Mater. Interfaces* **2020**, *12* (11), 12874−12882.

(27) Li, J.; Li, H.; Stone, W.; Weber, R.; Hy, S.; Dahn, J. R. Synthesis of Single Crystal LiNi0.5Mn0.3Co0.2O2for Lithium Ion Batteries. *J. Electrochem. Soc.* **2017**, *164* (14), A3529−A3537.

(28) Fan, X.; Hu, G.; Zhang, B.; Ou, X.; Zhang, J.; Zhao, W.; Jia, H.; Zou, L.; Li, P.; Yang, Y. Crack-free single-crystalline Ni-rich layered NCM cathode enable superior cycling performance of lithium-ion batteries. *Nano Energy* **2020**, *70*, 104450.

(29) Jiang, W.; Fan, X.; Zhu, X.; Wu, Z.; Li, Z.; Huang, R.; Zhao, S.; Zeng, X.; Hu, G.; Zhang, B.; Zhang, S.; Zhu, L.; Yan, L.; Ling, M.; Wang, L.; Liang, C. Well-dispersed single-crystalline nickel-rich cathode for long-life high-voltage all-solid-state batteries. *J. Power Sources* **2021**, *508*, 230335.

(30) Li, H.; Li, J.; Zaker, N.; Zhang, N.; Botton, G. A.; Dahn, J. R. Synthesis of Single Crystal LiNi0.88Co0.09Al0.03O2 with a Two-Step Lithiation Method. *J. Electrochem. Soc.* **2019**, *166* (10), A1956−A1963.

(31) Li, H.; Li, J.; Ma, X.; Dahn, J. R. Synthesis of Single Crystal LiNi0.6Mn0.2Co0.2O2with Enhanced Electrochemical Performance for Lithium Ion Batteries. *J. Electrochem. Soc.* **2018**, *165* (5), A1038−A1045.

(32) Qian, G.; Zhang, Y.; Li, L.; Zhang, R.; Xu, J.; Cheng, Z.; Xie, S.; Wang, H.; Rao, Q.; He, Y.; Shen, Y.; Chen, L.; Tang, M.; Ma, Z.-F. Single-crystal nickel-rich layered-oxide battery cathode materials: synthesis, electrochemistry, and intra-granular fracture. Energy Storage. *Materials* **2020**, *27*, 140−149.

(33) Trevisanello, E.; Ruess, R.; Conforto, G.; Richter, F. H.; Janek, J. Polycrystalline and Single Crystalline NCM Cathode Materials—Quantifying Particle Cracking, Active Surface Area, and Lithium Diffusion. *Adv. Energy Mater.* **2021**, *11* (18), 2003400.

(34) Ge, M.; Lee, W.-K. PyXAS − an open-source package for 2D X-ray near-edge spectroscopy analysis. *J. Synchrotron Radiat.* **2020**, *27* (2), 567−575.

(35) Zhang, F.; Lou, S.; Li, S.; Yu, Z.; Liu, Q.; Dai, A.; Cao, C.; Toney, M. F.; Ge, M.; Xiao, X.; et al. Surface regulation enables high stability of single-crystal lithium-ion cathodes at high voltage. *Nat. Commun.* **2020**, *11* (1), 3050.

(36) Lin, R.; Zhang, R.; Wang, C.; Yang, X. Q.; Xin, H. L. TEMImageNet training library and AtomSegNet deep-learning models for high-precision atom segmentation, localization, denoising, and deblurring of atomic-resolution images. *Sci. Rep.* **2021**, *11* (1), 5386.

(37) Yan, P.; Zheng, J.; Liu, J.; Wang, B.; Cheng, X.; Zhang, Y.; Sun, X.; Wang, C.; Zhang, J.-G. Tailoring grain boundary structures and chemistry of Ni-rich layered cathodes for enhanced cycle stability of lithium-ion batteries. *Nature Energy* **2018**, *3* (7), 600−605.

(38) Mao, Y.; Wang, X.; Xia, S.; Zhang, K.; Wei, C.; Bak, S.; Shadike, Z.; Liu, X.; Yang, Y.; Xu, R.; Pianetta, P.; Ermon, S.; Stavitski, E.; Zhao, K.; Xu, Z.; Lin, F.; Yang, X.-Q.; Hu, E.; Liu, Y. High-Voltage Charging-Induced Strain, Heterogeneity, and Micro-Cracks in Secondary Particles of a Nickel-Rich Layered Cathode Material. *Adv. Funct. Mater.* **2019**, *29* (18), 1900247.

(39) Besli, M. M.; Xia, S.; Kuppan, S.; Huang, Y.; Metzger, M.; Shukla, A. K.; Schneider, G.; Hellstrom, S.; Christensen, J.; Doeff, M. M.; Liu, Y. Mesoscale Chemomechanical Interplay of the LiNi0.8Co0.15Al0.05O2 Cathode in Solid-State Polymer Batteries. *Chem. Mater.* **2019**, *31* (2), 491−501.